Nano Research
2024, 17(3): 1107–1113

ISSN 1998-0124 CN 11-5974/O4
https://doi.org/10.1007/s12274-023-5913-6

Research Article

Suppressing the lattice oxygen diffusion via high-entropy oxide construction towards stabilized acidic water oxidation

Jing Ni[1,2], Zhaoping Shi[1,2], Yibo Wang[1,2], Jiahao Yang[1,2], Hongxiang Wu[1,2], Pengbo Wang[1,2], Kai Li[3], Meiling Xiao[1,2] (✉), Changpeng Liu[1,2] (✉), and Wei Xing[1,2] (✉)

[1] *State Key Laboratory of Electroanalytic Chemistry, Jilin Province Key Laboratory of Low Carbon Chemistry Power, Changchun Institute of Applied Chemistry, Chinese Academy of Sciences, Changchun 130022, China*
[2] *School of Applied Chemistry and Engineering, University of Science and Technology of China, Hefei 230026, China*
[3] *State Key Laboratory of Rare Earth Resource Utilization, Changchun Institute of Applied Chemistry, Chinese Academy of Sciences, Changchun 130022, China*

Received: 11 April 2023 / **Revised:** 29 May 2023 / **Accepted:** 11 June 2023

ABSTRACT

The scale-up deployment of ruthenium (Ru)-based oxygen evolution reaction (OER) electrocatalysts in proton exchange membrane water electrolysis (PEMWE) is greatly restricted by the poor stability. As the lattice-oxygen-mediated mechanism (LOM) has been identified as the major contributor to the fast performance degradation, impeding lattice oxygen diffusion to inhibit lattice oxygen participation is imperative, yet remains challenging due to the lack of efficient approaches. Herein, we strategically regulate the bonding nature of Ru–O towards suppressed LOM via Ru-based high-entropy oxide (HEO) construction. The lattice disorder in HEOs is believed to increase migration energy barrier of lattice oxygen. As a result, the screened $Ti_{23}Nb_9Hf_{13}W_{12}Ru_{43}O_x$ exhibits 11.7 times slower lattice oxygen diffusion rate, 84% reduction in LOM ratio, and 29 times lifespan extension compared with the state-of-the-art RuO_2 catalyst. Our work opens up a feasible avenue to constructing stabilized Ru-based OER catalysts towards scalable application.

KEYWORDS

ruthenium-based high-entropy oxide, suppressing the lattice oxygen diffusion, acidic oxygen evolution reaction

1 Introduction

Proton exchange membrane water electrolysis (PEMWE) for hydrogen production coupled with renewable energy offers an ideal solution to achieve the goal of net zero carbon emissions [1]. Despite numerous innate advantages such as high purity H_2 delivering, high energy efficiency, and compatibility with intermittent renewable energy [2–4], the scale-up adoption of PEMWE is seriously restricted by the sluggish oxygen evolution reaction (OER) in the anode [5, 6]. To date, iridium (Ir)-based catalysts are deemed as the state-of-the-art option in the commercial PEMWE devices [7–9]. However, the high cost (US \$60,670 kg^{-1}), scarcity, and low intrinsic activity of Ir limit their practical implementation and thus trigger enormous research enthusiasm in exploiting alternatives to Ir-based catalysts [10]. In this regard, Ru-based catalysts, with high intrinsic OER catalytic activity and lower cost (US \$9,523 kg^{-1}), have been hailed as the most promising candidate to replace Ir and attracted increasing attention in the past few years [11, 12].

In spite of the significant activity enhancement achieved, Ru-based catalysts suffer from severe performance degradation under harsh anodic and acidic conditions, showing an insufficient lifespan of few hours [13–17]. Combining advanced *operando* characterization techniques with theoretical calculations, it is recognized that the lattice-oxygen-mediated mechanism (LOM) accounts for the instability of Ru-based catalysts [18–21]. In the LOM progress, lattice oxygen is involved in the reaction pathway [22], accompanying with the migration of the atoms in the bulk phase including the lattice oxygen migration and proceeds with oxygen vacancies (Ov) formation, structural destruction, and detaching of active Ru moieties [23]. Such a LOM induces degradation of electrocatalysts. On this basis, either regulating the electronic structure of Ru to inhibit the redox of lattice oxygen or retarding the migration of lattice oxygen to avoid the formation of Ov in the bulk is capable of mitigating the LOM induced attenuation. Most of the recent endeavors were paid to stabilizing Ru-based oxides through the former strategy. For instance, noble metals (Pt [24], Ir [25], etc.), acid-insoluble metals (W [26]), and rare earth metals (Ce [27], Er [26], etc.) have been coupled with Ru to downshift the Ru d-band center towards decreased Ru–O bonding covalency. However, rare efforts have been devoted to mitigating or avoiding the migration of lattice oxygen due to the lack of efficient strategies for directly adjusting the migration energy barrier of lattice oxygen (thus migration rate). Thus, it is urgently desirable to develop innovative approaches to inhibiting lattice oxygen migration towards enhanced operational stability of Ru-based catalysts.

Motivated by this challenge, we strategically regulate the diffusion rate of lattice oxygen through constructing Ru-based high-entropy alloy oxide (HEO) electrocatalysts, in which the

Address correspondence to Meiling Xiao, mlxiao@ciac.ac.cn; Changpeng Liu, liuchp@ciac.ac.cn; Wei Xing, xingwei@ciac.ac.cn

oxygen migrating energy is proposed to be highly correlated with the lattice distortion. As a proof-of-concept study, alloy oxides with different elemental components are successfully synthesized with a modified molten salt oxidation method. Combining isotope labeled *in situ* differential electrochemical mass spectrum (DEMS) with first-principles calculations, we find the more elements in the alloy oxides (thus higher entropy), the higher energy barrier for migrating of lattice oxygen, attributable to the sluggish diffusion effect in HEOs. As a result, the optimized $Ti_{23}Nb_9Hf_{13}W_{12}Ru_{43}O_x$ (denoted as 5e HEOs) exhibits an lattice oxygen diffusion rate 11.7 times slower than that of RuO_2 and a resulting 29 times lifespan extension. Our work not only provides a highly stable Ru-based OER electrocatalyst but also enlightens the new version of inhibiting lattice oxygen participation in OER from the perspective of modulating the structure of lattice oxygen.

2 Experimental details

Chemicals. All chemicals were obtained from commercial suppliers and used as received without further purification. Potassium titanium oxide oxalate dihydrate ($C_4K_2O_9Ti$), hafnium chloride ($HfCl_4$), zinc nitrate hexahydrate ($Zn(NO_3)_2{\cdot}6H_2O$) and water-^{18}O ($H_2{}^{18}O$, 97 at.% ^{18}O) were purchased from Aladdin. Ammonium niobate oxalate hydrate ($C_4H_4NNbO_9{\cdot}nH_2O$) was purchased from Macklin Biochemical Technology Co., Ltd. Hexaammonium heptamolybdate tetrahydrate ($(NH_4)Mo_7O_2{\cdot}4H_2O$) were obtained from Xilong Chemical Co., Ltd. Ammonium Tungstate ($(MH_4)_6H_5[H_2(WO_4)_6]{\cdot}H_2O$) was obtained from Shanghai Reagent Factory. Ruthenium trichloride anhydrous was purchased from 3A Chemical. Sodium nitrate ($NaNO_3$) was obtained from Beijing F&F Chemical Co., Ltd. Carbon paper was obtained from Engineered Fibers Technology, LLC. 5 wt.% Nafion® ionomer was purchased from DuPont Co.

Preparation of alloy oxides. The alloy oxide was fabricated via a direct annealing method assisted by molten salt. Typically, for $Ti_{23}Nb_9Hf_{13}W_{12}Ru_{43}O_x$, the metal source preconfigured as an aqueous solution was uniformly mixed in accordance with the molar ratio almost consistent with the above molecular formula. Then the nitrate including $NaNO_3$ and $Zn(NO_3)_2$ were added to the above solution and stirred for 3 h. After rotary evaporation, the obtained precursor was annealed at 400 °C for 0.5 h. Finally, the annealed precursor was washed with 1 M HCl solution under ultrasound and deionized water then separated by suction filtration. After drying, the five-element high-entropy alloy oxide (5e HEOs, $Ti_{23}Nb_9Hf_{13}W_{12}Ru_{43}O_x$) can be obtained. Although $NaNO_3$ was added in larger quantities, the Na element added was effectively removed, as shown in Fig. S1 in the Electronic Supplementary Material (ESM) (the content of Na elements decreased from 40.94 wt.% to 0.31 wt.% after washing), so the final composition of the catalyst did not contain Na element. Other alloy oxides of different elements were prepared similarly, the difference was the type of metal source added and the molar ratio of the metal (for ease of comparison, other elemental alloy oxides are recorded as 4e EOs, 3e EOs, and 2e EOs for $Ti_{56}Nb_{10}Hf_{15}Ru_{19}O_x$, $Ti_{58}Nb_{19}Ru_{23}O_x$, and $Ti_{92}Ru_8O_x$, respectively. The commercial RuO_2 (recorded as Com. RuO_2) was used for comparison.

Structural characterizations. X-ray diffraction (XRD) patterns were collected using a D8 ADVANCE diffractometer (Germany BRUKER Company) with a Cu Kα (λ = 0.154 nm) radiation source in the 2θ range of 5°–90°. Scanning electron microscopy (SEM) was performed on a Philips XL 30 ESEMFEG scanning electron microscope. Transmission electron microscopy (TEM) and elemental mapping analysis were conducted on a FEI Titan 80-300 scanning transmission electron microscopy (STEM). High-resolution TEM (HRTEM) and energy dispersive X-ray (EDX) elemental mapping were conducted in a JEM-F200 field emission transmission electron microscope. Textural properties such as specific surface area were determined through N_2 gas adsorption/desorption measurements (ASAP 2020, Micromeritics Instrument Corporation, USA). The surface electronic states were determined by X-ray photoelectron spectroscopy (XPS) using a Thermo Fisher Scientific ESCALAB 250Xi unit with Al-Kα ($h\nu$ = 1486.6 eV) as the X-ray source. Inductively coupled plasma optical emission spectroscopy (ICP-OES; ThermoScientific iCAP6300) was used to determine the ratio of metal atoms in each alloy oxides and dissolution ratio of Ru during stability tests.

Electrochemical measurements in a three-electrode cell. The electrocatalytic measurements of as-prepared catalysts were performed using a standard three-electrode cell on Princeton PARSTAT MC. Typically, a gold electrode with a diameter of 3 mm coated with each catalyst was used as the working electrode. A mercurous sulfate electrode (Hg/Hg_2SO_4, filled with saturated K_2SO_4 solution) and a carbon rod were used as the reference electrode and counter electrode, respectively. 0.5 M H_2SO_4 was used as electrolyte. The Hg/Hg_2SO_4 reference electrode was calibrated in H_2-saturated 0.5 M H_2SO_4 solution by measuring hydrogen oxidation/evolution at a platinum wire electrode and defining the point of zero current as 0 V versus reversible hydrogen electrode (RHE). Therein, all of the measured potentials vs. Hg/Hg_2SO_4 were converted to the potential vs. RHE according to the following equation

$$E\,(\text{vs. RHE}) = E\,(\text{vs. Hg/Hg}_2\text{SO}_4) + C$$

where C is the potential difference between the Hg/Hg_2SO_4 reference electrode and RHE in 0.5 M H_2SO_4, which was calibrated by the open circuit potential (OCP) test prior to electrocatalysis. The calibration values (C) of the two reference electrodes we used were slightly different, 0.7052 and 0.7034 V, respectively.

The catalysts (5 mg) and Vulcan XC-72 (2.5 mg) were dispersed in a mixture of 0.45 mL ethanol and 50 μL Nafion® solution (5 wt.%). After ultrasonication, 2.52 μL homogeneous ink was dropped on a gold electrode (diameter 3 mm). Linear sweep voltammetry (LSV) curves of OER were obtained with a scan rate of 5 mV·s^{-1} with *iR* correction. Chronopotentiometry (CP) tests at 10 mA·cm^{-2} for catalysts were conducted on 0.5 cm × 1 cm carbon paper which was dropped with 50 μL catalyst ink.

***In situ* DEMS with isotope labeling.** *In situ* DEMS experiments were performed on an *in situ* differential electrochemical mass spectrometer purchased from Linglu Instruments (Shanghai) Co., Ltd. Typically, the test was carried out in a three-electrode cell with 0.5 M H_2SO_4 as electrolyte. The catalyst ink was prepared and dropped on a gold electrode. The oxygen in the alloy oxide catalysts was labeled as ^{18}O by chronopotential test with $H_2{}^{18}O$. After removing the $H_2{}^{18}O$ on the surface of electrode and drying, the DEMS experiments were performed. The mass signal of $^{34}O_2/^{32}O_2$ is defined as the ratio of $^{34}O_2$ signal to $^{32}O_2$ signal at the onset time of oxygen evolution reaction obtained by mathematical fitting calculation.

3 Results and discussion

Alloy oxides were obtained via a direct annealing method assisted by molten salt. The schematic diagram of the process for preparing optimized high-entropy alloy oxide (5e HEOs, $Ti_{23}Nb_9Hf_{13}W_{12}Ru_{43}O_x$) is depicted in Fig. 1(a) (see methods for experimental details). For convenient comparison, alloy oxides with different element numbers are denoted as 4e EOs, 3e EOs, and 2e EOs for $Ti_{56}Nb_{10}Hf_{15}Ru_{19}O_x$, $Ti_{58}Nb_{19}Ru_{23}O_x$, and

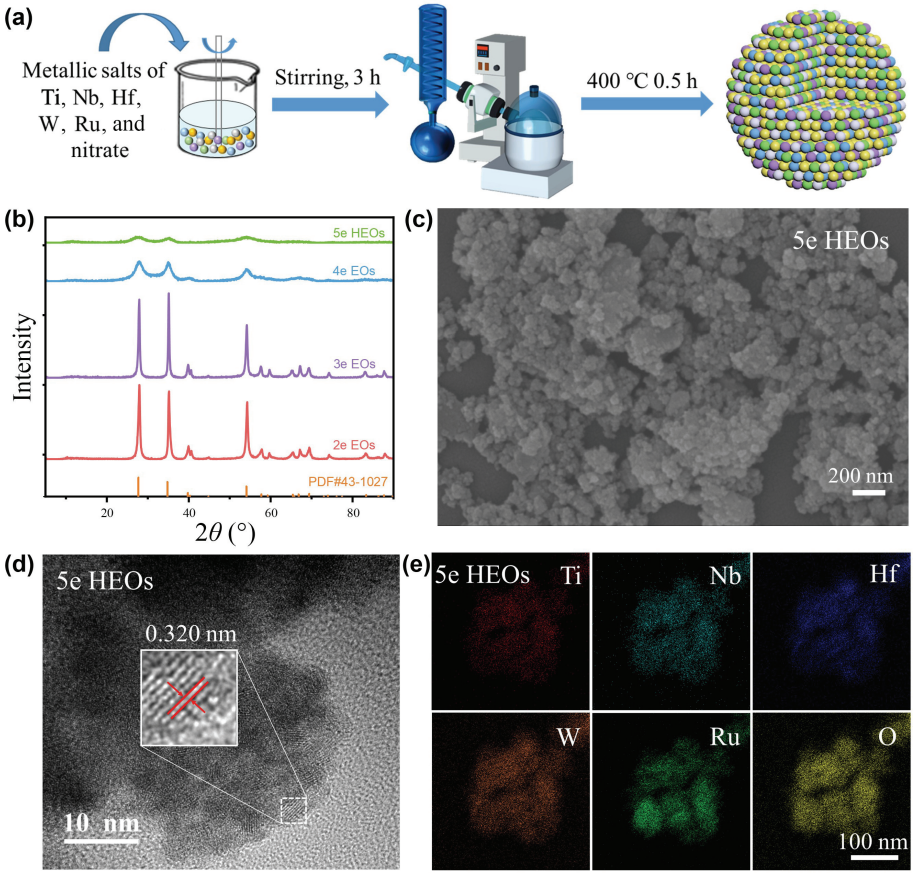

Figure 1 Preparation scheme and physical structure of alloy oxides: (a) schematic figure for preparation of five-element high-entropy alloy oxides; (b) X-ray diffraction patterns of different alloy oxides; (c) SEM image for 5e HEOs; (d) HRTEM image of 5e HEOs; (e) EDX mapping of 5e HEOs.

$Ti_{92}Ru_8O_x$, respectively. The atomic ratio in each alloy oxide was confirmed by ICP-OES measurement (Table S1 in the ESM). To determine the crystallographic structure of as-prepared alloy oxides, Powder X-ray diffraction (XRD) was carried out. As shown in Fig. 1(b), all diffraction peaks were well indexed to the standard pattern of JCPDS-43-1027, without any characteristic peak corresponding to MO_x (M = Ti, Nb, Hf, W), confirming the successful formation of phase-pure tetragonal structure alloy oxides. Notably, the diffraction peaks appear broader with increased elements number, indicating the smaller particle size according to the Debye–Scherrer equation (Fig. S2(a) in the ESM). Then, the nanostructure of alloy oxides was examined by SEM and TEM. As shown in Fig. 1(c), the SEM image of 5e HEOs reveals an accumulational nanocrystalline morphology with a size of 40 nm. The TEM images (Fig. S2(b) in the ESM) reveal that the nanocrystalline is composed of grains with a size of 2.2 nm for 5e HEOs, which is in line with the results from XRD. The TEM images of alloy oxides (Figs. S2(c)–S2(e) in the ESM) show that the agglomerates are fragmented into uniform aggregates with increased element types, which may originate from the modified crystal nucleation/growth behaviors as observed in other solid-solution systems [27]. The interplanar spacing at 0.320 nm is clearly observed in the HRTEM image of 5e HEOs (Fig. 1(d)), exhibiting slight increasing spacing compared to the (110) facets (0.318 nm) of rutile RuO_2. This is consistent with the characteristics introduced by other metal atoms with larger radii and consistent with the XRD pattern shown in Fig. 1(b). The EDX elemental mapping of alloy oxides (Fig. 1(e) and Fig. S3 in the ESM) demonstrates that each element is evenly distributed in the catalyst nanostructures. Taking all these together, the successful preparation of series of single-phase alloy oxides with uniform element dispersion is confirmed.

The OER catalytic performance of as-prepared alloy oxides was evaluated and compared to that of commercial RuO_2 in a conventional three-electrode set-up, with 0.5 M H_2SO_4 as electrolyte. LSV curves of all samples with the same catalyst mass loading were first collected to probe the OER activity. As shown in Fig. 2(a), the apparent activity of alloy oxides increases with incorporation of more types of elements. The optimized 5e HEOs exhibits the highest OER activity, requiring only a 251 mV overpotential to attain 10 $mA{\cdot}cm^{-2}$, which is 61 mV lower than that of Com. RuO_2. Besides, the alloy oxides except for Ru elements (denoted as $TiNbHfWO_x$, $TiNbHfO_x$, and $TiNbO_x$) were prepared and their structure and activity were illustrated by XRD, SEM, EDX, and LSV curves as shown in Fig. S4, Table S2 and Section S1 in the ESM. These alloy oxides attain a current density of less than 1 $mA{\cdot}cm^{-2}$ at 1.65 V potential versus RHE, indicating that Ru is still the main active center in high-entropy alloy oxide, and the addition of other non-precious metals mainly plays a regulating role in improving the activity. After normalized to the electrochemically active surface area (ECSA, obtained from Fig. S5 in the ESM), the optimized 5e HEOs also present a higher intrinsic activity of 25 $\mu A{\cdot}cm_{ECSA}^{-2}$ at 1.5 V (vs. RHE), which is 2 times that of Com. RuO_2 (Fig. 2(b)). In addition, the Tafel slope of 5e HEOs is as low as 65 $mV{\cdot}dec^{-1}$, significantly lower than those of other alloy oxides and Com. RuO_2 (72–134 $mV{\cdot}dec^{-1}$) (Fig. S6(a) in the ESM), indicating accelerated OER kinetics on the 5e HEOs. In line with the Tafel analysis, electrochemical impedance spectra (EIS) suggest faster charge transfer rate on the 5e HEOs than on other alloy catalysts (Fig. S6(b), Section S2 and Table S3 in the ESM).

To evaluate the operational stability of the as-prepared alloy oxides, chronopotentiometric (CP) tests were performed at a constant current density of 10 $mA{\cdot}cm^{-2}$. The 5e HEOs retains the activity within 25 h uninterrupted operation, with a slight potential increase (from 1.50 to 1.57 V, Fig. 2(c) and Fig. S6(c) in

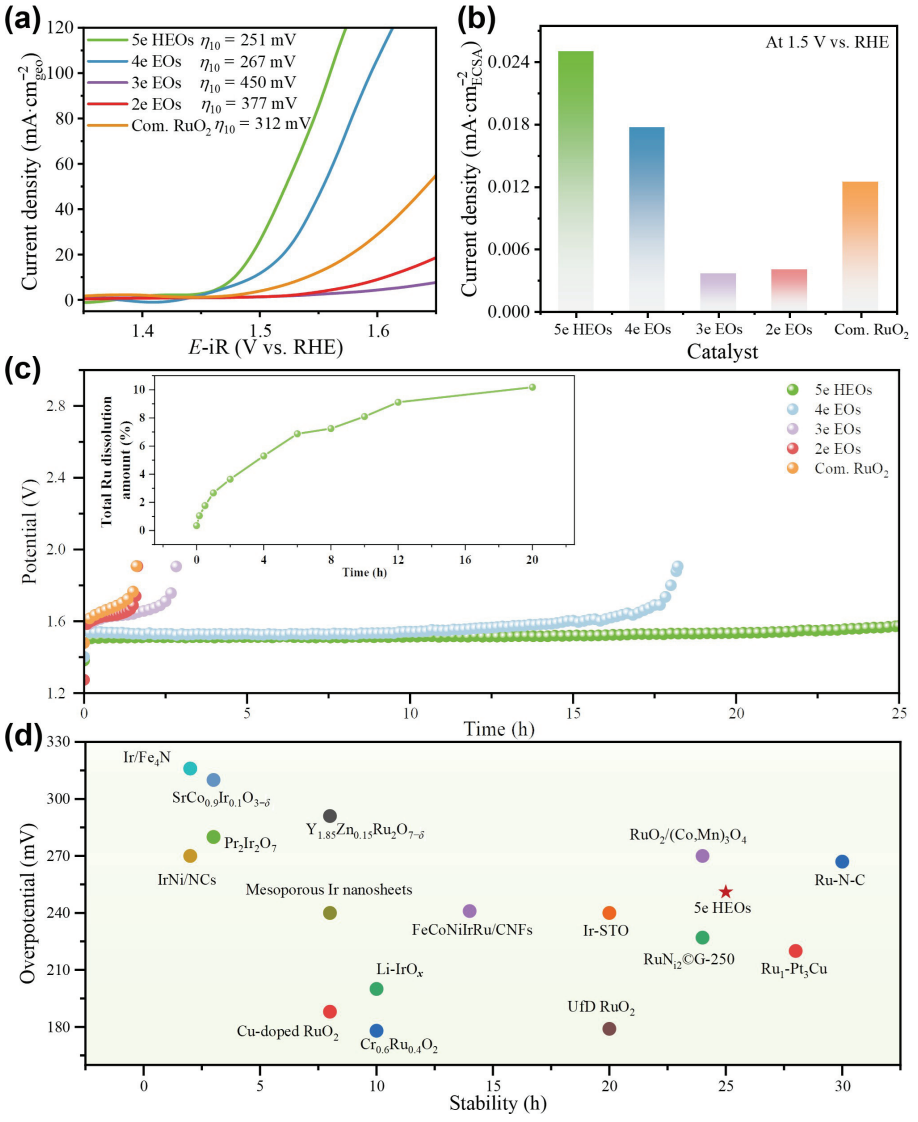

Figure 2 Comparison of electrocatalytic performance: (a) geometric area normalized LSV curves for as-prepared alloy oxide catalysts and Com. RuO_2; (b) current density normalized for ECSA of prepared alloy oxide catalysts and Com. RuO_2 at 1.5 V (vs. RHE); (c) chronopotentiometry curves for as-prepared alloy oxides catalysts and Com. RuO_2, with the inset showing the proportion of total Ru dissolution; (d) comparison of OER performance (overpotential at 10 mA·cm^{-2}) and operational stability (operation time) of 5e HEOs with reported anode catalysts, activity, and stability data are derived from Table S4 in the ESM.

the ESM). In sharp contrast, the OER activities of 4e EOs, 3e EOs, 2e EOs, and Com. RuO_2 decrease dramatically during the CP test, giving the lifetimes of only 18.21, 2.82, 1.64, and 1.60 h, respectively. To investigate the origins of the enhanced stability of 5e HEOs, we monitored its dissolution behavior under OER conditions by measuring Ru concentration in the electrolyte during 20-h CP measurement via ICP-OES. As shown in the inset of Fig. 2(c), the dissolution rate of Ru gradually decreases with elongated operational time and converges to 1.13 μg·h^{-1} at 20 h. More directly, SEM, XRD, and XPS results (Figs. S7(a)–S7(c) in the ESM) before and after the durability test show that the bulk and surface crystalline structure of 5e HEOs remain intact, implying the inherently robust nature of 5e HEOs. The LSV curves of 5e HEOs before and after the stability test show no significant attenuation of activity during the CP test (Fig. S7(d) in the ESM). Additionally, the stability number (S-number) and lifetime of 5e HEOs are calculated to be 4.16 × 10^3 and 441 h, which is 29 times that of Com. RuO_2 (1.43 × 10^2, 15 h), further proving the significance of constructing high-entropy alloy oxides on improving stability (calculation methods shown in the ESM). Besides, the optimized 5e HEOs also exhibits coordinated OER activity and stability compared to those advanced catalysts recently reported (Fig. 2(d) and Table S4 in the ESM).

To rationalize the origin of the stability of 5e HEOs, the reactivity of O was carefully analyzed by *in situ* DEMS and XPS. To validate the suppressed LOM in rationally designed high-entropy alloy oxide system, we first carried out *in situ* ^{18}O isotope-labeling DEMS measurements with Com. RuO_2 as control. The schematic of *in situ* DEMS measurements is shown in Fig. 3(a). The samples were labeled with ^{18}O isotopes in 0.5 M H_2SO_4 aqueous electrolyte and tested in 0.5 M ^{16}O-labelled H_2SO_4 aqueous electrolyte, with the mass intensity of m/z = 32 and m/z = 34 monitored (Fig. 3(b) and Fig. S8 in the ESM). The ratio of $^{34}O_2/^{32}O_2$ in the gas products of Com. RuO_2 is calculated to be 18.2% at the onset potential, implying a LOM content of 9.1% during OER. On the contrary, the isotope-labeled 5e HEOs gives a $^{34}O_2/^{32}O_2$ ratio of 2.9%, indicating the LOM path is suppressed in 5e HEOs (Fig. 3(c)). The reactivity of lattice oxygen during OER was assessed, and the evolution on the ratio of O_V in 5e HEOs after the stability test was firstly studied by XPS. As shown in Fig. S9(a) in the ESM, the ratio of O_L/O_V in the O 1s XPS spectrum of 5e HEOs coated on carbon paper keeps consistent at ~ 0.310 before and after the galvanostatic test, also indicating less LOM during OER and thus no significant increase in oxygen vacancy density after OER.

We turned to elucidate the intrinsic mechanism of LOM

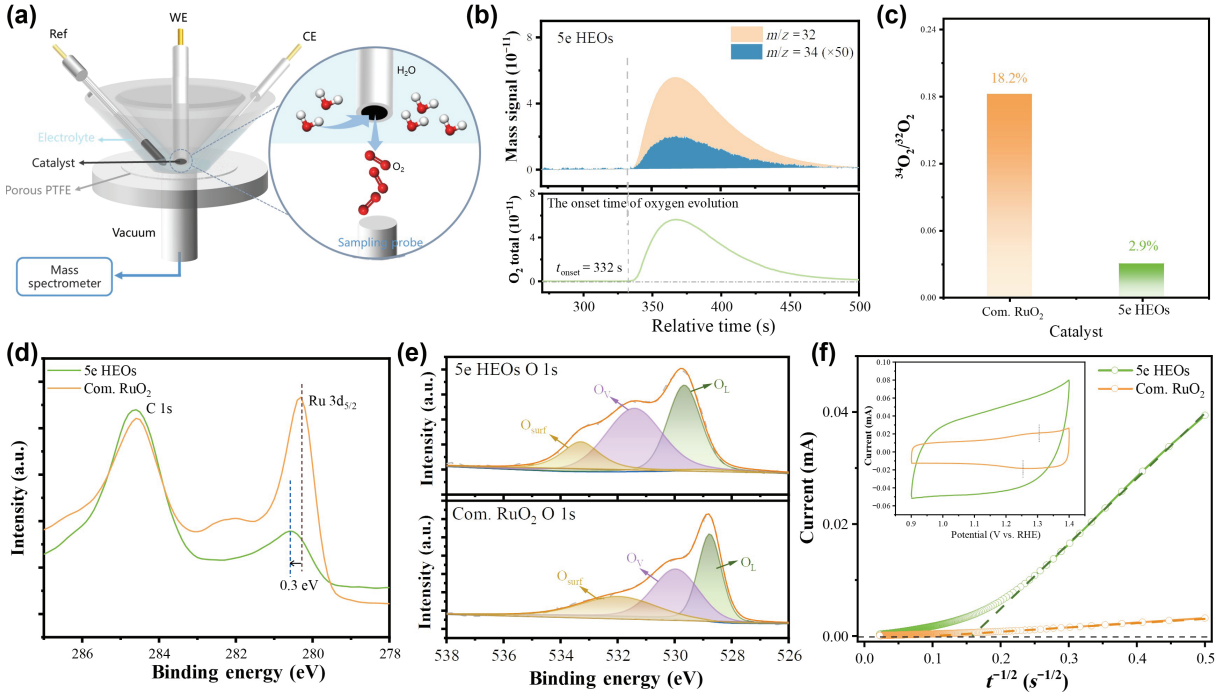

Figure 3 The origin of the stability of 5e HEOs: (a) schematic of *in situ* DEMS; (b) determination of the onset time of oxygen evolution and DEMS measurements of $^{34}O_2$ and $^{32}O_2$ signals from the reaction products for 5e HEOs in 0.5 M H_2SO_4 in $H_2{}^{16}O$; (c) comparison of the ratio of $^{34}O_2/^{32}O_2$ in the gas products for Com. RuO_2 and 5e HEOs; (d) high-resolution XPS spectra of Ru 3d for 5e HEOs and Com. RuO_2; (e) the deconvoluted O 1s spectra for 5e HEOs and Com. RuO_2; (f) chronoamperometry data (i vs. $t^{-1/2}$) used for the calculation of oxygen ion diffusion coefficient. The inset shows the CV curves of 5e HEOs and Com. RuO_2 in Ar-saturated 0.5 M H_2SO_4 solution at a scan rate of 20 mV·s^{-1}.

inhibition by analyzing the states of Ru and O in 5e HEOs. As shown in Fig. 3(d), a 0.3 eV positive shift in the binding energy (280.6 eV) of $3d_{5/2}$ XPS spectrum of 5e HEOs is observed compared to that of commercial RuO_2 (280.3 eV) in the high-resolution Ru 3d spectrum, suggesting a lower electron density and an increased oxidation state of Ru in 5e HEOs electrocatalysts [13]. Further, the high-resolution O 1s XPS spectra were recorded (Fig. 3(e)) to monitor the structure evolution of lattice oxygen after constructing HEOs. Obviously, the peaks of lattice oxygen (O_L), oxygen vacancy (O_V), and surface oxygen (O_{surf}) [14] in 5e HEOs shift to higher binding energies compared with those of Com. RuO_2, indicating the enhanced Ru–O bond covalency in high-entropy alloy oxides. The projected density of states (PDOS) plots of the Ru d band in 5e HEOs and RuO_2 also show the reduced electronic density in the Ru site and higher d-band center in 5e HEOs (Fig. S9(b) in the ESM), which is in well accordance with the higher Ru oxidation states. However, it is inconsistent with the conventional understanding that higher Ru oxidation states and enhanced Ru–O bond covalency are indicative to the activation of lattice oxygen during OER [15, 24, 28]. This contradiction indirectly implies that it is the suppressed oxygen reactivity/migration kinetics rather than tailored electronic states of Ru that results in the inhibited LOM.

To validate this hypothesis, we further carried out oxygen intercalation measurements to estimate the oxygen ion diffusion coefficients (D_O) [29] of 5e HEOs and Com RuO_2 (Fig. 3(f) and Fig. S10 in the ESM). According to the three-dimensional diffusion model reported before [30–32], the D_O value of Com. RuO_2 is calculated to be 5.43×10^{-15} cm^2·s^{-1}. Remarkably, 5e HEOs has a D_O of 4.64×10^{-16} cm^2·s^{-1}, which is ~ 11.7 times slower than that of Com. RuO_2 (Table S5 in the ESM). Thus, it is unambiguous that the suppressed LOM is originated from the restrained oxygen ion diffusion derived from the lattice distortion in high-entropy alloy oxides [33].

For in-depth understanding the relation between alloy oxide structure, the reactivity of lattice oxygen and catalytic stability, we further conducted *in situ* DEMS on alloy oxides with various element numbers. After labeled with ^{18}O, the signals of $^{34}O_2$ and $^{32}O_2$ in the products catalyzed by alloy oxides were monitored (Fig. S8 in the ESM). As indicated by the $^{34}O_2/^{32}O_2$ ratios of different alloy oxides (Fig. 4(a)), the proportion of lattice oxygen participation during OER decreases quickly with increased element number, i.e., from 6.4% for 2e EOs to 1.5% for 5e HEOs. Besides, the LOM ratio of alloy oxides is correlated linearly with the OER stability (Fig. 4(b)). Notably, the operational duration time of 5e HEOs is 15.2 times longer than that of 2e EOs with higher LOM content. Giving the high uniformity between oxygen ion diffusion coefficients, *in situ* DEMS, and CP test, we believe the boosting in electrocatalytic stability of 5e HEOs is attributable to the inhibited lattice oxygen participation associated with the sluggish diffusion kinetics of high-entropy alloy oxide during OER.

To further verify the effect of retarding lattice oxygen diffusion on enhancing the OER stability, DFT calculations were performed. Two structure models, i.e., ideal rutile RuO_2 and 5e HEOs (Fig. S11 in the ESM) with different types of oxygen vacancy (Fig. S12 in the ESM) were selected for consideration. Based on the experimental results obtained above, the diffusion rate of lattice oxygen, which is determined by the energy barrier for lattice oxygen migration, plays a vital role in the stability of LOM. Thus, the energy barriers for different lattice oxygen in HEOs (including Ti-O-Ru, Nb-O-Ru, Hf-O-Ru, W-O-Ru) and RuO_2 (Ru-O-Ru) migrated to the surface were calculated and compared in Table S6 in the ESM. Clearly, the migration energies of the four types of lattice oxygen considered in 5e HEOs (0.17, −0.37, −0.67, and −0.20 eV) are higher than those of the lattice oxygen in RuO_2 (−0.79 and −0.82 eV), which results in the decreased oxygen ion diffusion rate, lower ratio of LOM and thus enhanced stability (Fig. 4(c)). Together with the experimental and computational results, we confirm that the improved operational stability of 5e HEOs is derived from the large migration energy barrier of lattice oxygen, which is caused by the lattice disorder in high-entropy alloy oxides.

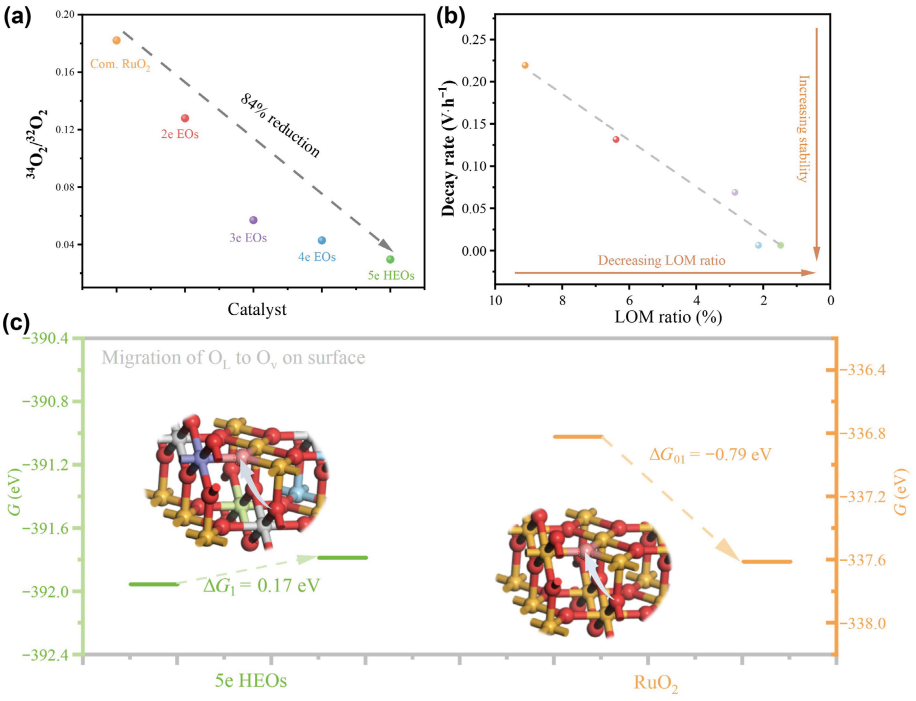

Figure 4 Comprehension of the origin of the enhanced stability: (a) comparison of the ratio of $^{34}O_2/^{32}O_2$ in the gas products for alloy oxides; (b) the relationship of the content for lattice oxygen participating in OER with catalytical stability (indicated by decay rate of catalysts in the beginning 1.6 h of CP test); (c) comparison of migration energies of lattice oxygen for 5e HEOs and RuO_2.

4 Conclusions

In summary, we presented an innovative and feasible idea, namely commanding the migration of lattice oxygen, to address the stability issue associated with Ru-based electrocatalysts for OER, which is accomplished by constructing high-entropy alloy oxides. As expected, the screened five-element high-entropy alloy oxides ($Ti_{23}Nb_9Hf_{13}W_{12}Ru_{43}O_x$) exhibited 29 times lifetime extension compared with Com. RuO_2. Based on the experiment and DFT calculations, we revealed that the superb stability of the as-designed $Ti_{23}Nb_9Hf_{13}W_{12}Ru_{43}O_x$ catalyst is originated from the reduced LOM caused by low diffusion rates of lattice oxygen rather than by the modulated electronic structure of Ru. This work not only provides a highly competitive Ru-based OER catalyst with excellent stability, but also opens up a new avenue to inhibiting lattice oxygen participation in OER from the perspective of modulating the structure of lattice oxygen.

Acknowledgements

The authors thank the National Key R&D Program of China (No. 2021YFB4000200), the National Natural Science Foundation of China (No. 22232004), the Strategic Priority Research Program of the Chinese Academy of Sciences (No. XDA21090400), and the Jilin Province Science and Technology Development Program (Nos. 20210301008GX, YDZJ202202CXJD011, and 20210502002ZP) for financial support.

Electronic Supplementary Material: Supplementary material (further details of the lattice oxygen ion diffusion coefficients measurement, determination of the ECSA, S-number and lifetime, additional TEM images and EDX-mapping images, additional XPS spectra, the corresponding electrocatalytic curves, and models for DFT calculations) is available in the online version of this article at https://doi.org/10.1007/s12274-023-5913-6.

References

[1] Chen, J. Y.; Cui, P. X.; Zhao, G. Q.; Rui, K.; Lao, M. M.; Chen, Y. P.; Zheng, X. S.; Jiang, Y. Z.; Pan, H. G.; Dou, S. X. et al. Low-coordinate iridium oxide confined on graphitic carbon nitride for highly efficient oxygen evolution. *Angew. Chem., Int. Ed.* **2019**, *58*, 12540–12544.

[2] Wu, H.; Huang, Q. X.; Shi, Y. Y.; Chang, J. W.; Lu, S. Y. Electrocatalytic water splitting: Mechanism and electrocatalyst design. *Nano Res.*, in press, https://doi.org/10.1007/s12274-023-5502-8.

[3] Carmo, M.; Fritz, D. L.; Mergel, J.; Stolten, D. A comprehensive review on PEM water electrolysis. *Int. J. Hydrog. Energy.* **2013**, *38*, 4901–4934.

[4] Lagadec, M. F.; Grimaud, A. Water electrolysers with closed and open electrochemical systems. *Nat Mater.* **2020**, *19*, 1140–1150.

[5] Shi, Z. P.; Wang, X.; Ge, J. J.; Liu, C. P.; Xing, W. Fundamental understanding of the acidic oxygen evolution reaction: Mechanism study and state-of-the-art catalysts. *Nanoscale* **2020**, *12*, 13249–13275.

[6] Ni, J.; Shi, Z. P.; Wang, X.; Wang, Y. B.; Wu, H. X.; Liu, C. P.; Ge, J. J.; Xing, W. Recent development of low iridium electrocatalysts toward efficient water oxidation. *J. Electrochem.* **2022**, *28*, 2214010.

[7] Chen, X. J.; Liao, W. Y.; Zhong, M. X.; Chen, J. J.; Yan, S.; Li, W. M.; Wang, C.; Chen, W.; Lu, X. F. Rational design of robust iridium-ceria oxide-carbon nanofibers to boost oxygen evolution reaction in both alkaline and acidic media. *Nano Res.* **2023**, *16*, 7724–7732.

[8] Zhao, G. Q.; Luo, Z. X.; Zhang, B. H.; Chen, Y. P.; Cui, X. Z.; Chen, J.; Liu, Y. F.; Gao, M. X.; Pan, H. G.; Sun, W. P. Epitaxial interface stabilizing iridium dioxide toward the oxygen evolution reaction under high working potentials. *Nano Res.* **2023**, *16*, 4767–4774.

[9] Liu, Z. J.; Wang, G. J.; Guo, J. Y.; Wang, S. Y.; Zang, S. Q. Sub-2 nm IrO_2/Ir nanoclusters with compressive strain and metal vacancies boost water oxidation in acid. *Nano Res.* **2023**, *16*, 334–342.

[10] Hao, S. Y.; Sheng, H. Y.; Liu, M.; Huang, J. Z.; Zheng, G. K.; Zhang, F.; Liu, X. N.; Su, Z. W.; Hu, J. J.; Qian, Y. et al. Torsion strained iridium oxide for efficient acidic water oxidation in proton exchange membrane electrolyzers. *Nat. Nanotechnol.* **2021**, *16*, 1371–1377.

[11] Ji, M. W.; Yang, X.; Chang, S. D.; Chen, W. X.; Wang, J.; He, D. S.; Hu, Y.; Deng, Q.; Sun, Y.; Li, B. et al. RuO_2 clusters derived from bulk $SrRuO_3$: Robust catalyst for oxygen evolution reaction in acid. *Nano Res.* **2022**, *15*, 1959–1965.

[12] Yao, Q.; Yu, Z. Y.; Chu, Y. H.; Lai, Y. H.; Chan, T. S.; Xu, Y.; Shao, Q.; Huang, X. Q. S incorporated RuO_2-based nanorings for active and stable water oxidation in acid. *Nano Res.* **2022**, *15*, 3964–3970.

[13] Niu, S. Q.; Kong, X. P.; Li, S. W.; Zhang, Y. Y.; Wu, J.; Zhao, W. W.; Xu, P. Low Ru loading RuO_2/$(Co, Mn)_3O_4$ nanocomposite with modulated electronic structure for efficient oxygen evolution reaction in acid. *Appl. Catal. B: Environ.* **2021**, *297*, 120442.

[14] Zhang, L. J.; Jang, H.; Liu, H. H.; Kim, M. G.; Yang, D. J.; Liu, S. G.; Liu, X. E.; Cho, J. Sodium-decorated amorphous/crystalline RuO_2 with rich oxygen vacancies: A robust pH-universal oxygen evolution electrocatalyst. *Angew. Chem., Int. Ed.* **2021**, *60*, 18821–18829.

[15] Liu, C. J.; Sheng, B. B.; Zhou, Q.; Cao, D. F.; Ding, H. H.; Chen, S. M.; Zhang, P. J.; Xia, Y. J.; Wu, X. J.; Song, L. Motivating Ru-bri site of RuO_2 by boron doping toward high performance acidic and neutral oxygen evolution. *Nano Res.* **2022**, *15*, 7008–7015.

[16] Feng, Q.; Wang, Q.; Zhang, Z.; Xiong, Y. Y. H.; Li, H. Y.; Yao, Y.; Yuan, X. Z.; Williams, M. C.; Gu, M.; Chen, H. et al. Highly active and stable ruthenate pyrochlore for enhanced oxygen evolution reaction in acidic medium electrolysis. *Appl. Catal. B: Environ.* **2019**, *244*, 494–501.

[17] Lin, Y. C.; Tian, Z. Q.; Zhang, L. J.; Ma, J. Y.; Jiang, Z.; Deibert, B. J.; Ge, R. X.; Chen, L. Chromium-ruthenium oxide solid solution electrocatalyst for highly efficient oxygen evolution reaction in acidic media. *Nat. Commun.* **2019**, *10*, 162.

[18] Shi, Z. P.; Li, J.; Wang, Y. B.; Liu, S. W.; Zhu, J. B.; Yang, J. H.; Wang, X.; Ni, J.; Jiang, Z.; Zhang, L. J. et al. Customized reaction route for ruthenium oxide towards stabilized water oxidation in high-performance PEM electrolyzers. *Nat. Commun.* **2023**, *14*, 843.

[19] Zeng, F.; Mebrahtu, C.; Liao, L. F.; Beine, A. K.; Palkovits, R. Stability and deactivation of OER electrocatalysts: A review. *J. Energy Chem.* **2022**, *69*, 301–329.

[20] Wang, Z. B.; Guo, X. Y.; Montoya, J.; Nørskov, J. K. Predicting aqueous stability of solid with computed Pourbaix diagram using SCAN functional. *npj Comput. Mater.* **2020**, *6*, 160.

[21] Cherevko, S.; Geiger, S.; Kasian, O.; Kulyk, N.; Grote, J. P.; Savan, A.; Shrestha, B. R.; Merzlikin, S.; Breitbach, B.; Ludwig, A. et al. Oxygen and hydrogen evolution reactions on Ru, RuO_2, Ir, and IrO_2 thin film electrodes in acidic and alkaline electrolytes: A comparative study on activity and stability. *Catal. Today.* **2016**, *262*, 170–180.

[22] Ma, Y. Y.; An, Y. R.; Xu, Z.; Cheng, L. F.; Yuan, W. Y. Activating lattice oxygen of two-dimensional $M_nX_{n-1}O_2$ MXenes via zero-dimensional graphene quantum dots for water oxidation. *Sci. China Mater.* **2022**, *65*, 3053–3061.

[23] Grimaud, A.; Demortière, A.; Saubanère, M.; Dachraoui, W.; Duchamp, M.; Doublet, M. L.; Tarascon, J. M. Activation of surface oxygen sites on an iridium-based model catalyst for the oxygen evolution reaction. *Nat. Energy.* **2016**, *2*, 16189.

[24] Yao, Y. C.; Hu, S. L.; Chen, W. X.; Huang, Z. Q.; Wei, W. C.; Yao, T.; Liu, R. R.; Zang, K. T.; Wang, X. Q.; Wu, G. et al. Engineering the electronic structure of single atom Ru sites via compressive strain boosts acidic water oxidation electrocatalysis. *Nat. Catal.* **2019**, *2*, 304–313.

[25] Jiang, Y.; Mao, Y. N.; Jiang, Y. M.; Liu, H.; Shen, W.; Li, M.; He, R. X. Atomic equidistribution enhanced RuIr electrocatalysts for overall water splitting in the whole pH range. *Chem. Eng. J.* **2022**, *450*, 137909.

[26] Hao, S. Y.; Liu, M.; Pan, J. J.; Liu, X. N.; Tan, X. L.; Xu, N.; He, Y.; Lei, L. C.; Zhang, X. W. Dopants fixation of Ruthenium for boosting acidic oxygen evolution stability and activity. *Nat. Commun.* **2020**, *11*, 5368.

[27] He, J.; Li, W. Q.; Xu, P.; Sun, J. M. Tuning electron correlations of RuO_2 by co-doping of Mo and Ce for boosting electrocatalytic water oxidation in acidic media. *Appl. Catal. B: Environ.* **2021**, *298*, 120528.

[28] Lin, C.; Li, J. L.; Li, X. P.; Yang, S.; Luo, W.; Zhang, Y. J.; Kim, S. H.; Kim, D. H.; Shinde, S. S.; Li, Y. F. et al. *In-situ* reconstructed Ru atom array on α-MnO_2 with enhanced performance for acidic water oxidation. *Nat. Catal* **2021**, *4*, 1012–1023.

[29] Pan, Y. L.; Xu, X. M.; Zhong, Y. J.; Ge, L.; Chen, Y. B.; Veder, J. P. M.; Guan, D. Q.; O'Hayre, R.; Li, M. R.; Wang, G. X. et al. Direct evidence of boosted oxygen evolution over perovskite by enhanced lattice oxygen participation. *Nat. Commun.* **2020**, *11*, 2002.

[30] Mefford, J. T.; Rong, X.; Abakumov, A. M.; Hardin, W. G.; Dai, S.; Kolpak, A. M.; Johnston, K. P.; Stevenson, K. J. Water electrolysis on $La_{1-x}Sr_xCoO_{3-\delta}$ perovskite electrocatalysts. *Nat. Commun.* **2016**, *7*, 11053.

[31] van Buren, F. R.; Broers, G. H. J.; Bouman, A. J.; Boesveld, C. The electrochemical determination of oxygen ion diffusion coefficients in $La_{0.50}Sr_{0.50}CoO_{3-y}$. *J. Electroanal. Chem. Interfacial Electrochem.* **1978**, *88*, 353–361.

[32] van Buren, F. R.; Broers, G. H. J.; Bouman, A. J.; Boesveld, C. An electrochemical method for the determination of oxygen ion diffusion coefficients in $La_{1-x}Sr_xCoO_{3-y}$ compounds: Theoretical aspects. *J. Electroanal. Chem. Interfacial Electrochem.* **1978**, *87*, 389–394.

[33] Huang, X. F.; Yang, G. X.; Li, S.; Wang, H. J.; Cao, Y. H.; Peng, F.; Yu, H. Noble-metal-based high-entropy-alloy nanoparticles for electrocatalysis. *J. Energy Chem.* **2022**, *68*, 721–751.